Radio Science, Volume 36, Number 1, Pages 53–66, January–February 2001

Verification of a two-dimensional/three-dimensional hybrid ray-tracing method for spatiotemporal channel modeling

Houtao Zhu

Department of Information Processing, Tokyo Institute of Technology, Tokyo

Jun-ichi Takada and Kiyomichi Araki

Department of Electrical and Electronic Engineering, Tokyo Institute of Technology, Tokyo

Takehiko Kobayashi

YRP Mobile Telecommunications Key Technology Research Laboratories Co., Ltd., Yokosuka, Kanagawa, Japan

Abstract. Spatiotemporal channel modeling is fundamental to the design and implementation of future high-speed wireless communication systems. This paper investigates a two-dimensional–three-dimensional (2-D/3-D) hybrid ray-tracing method for outdoor microcellular and picocellular urban environments. It also explores the spatiotemporal channel model derived from this ray-tracing method. This 2-D/3-D ray-tracing method launches rays in a horizontal plane and establishes ray paths in three-dimensional (3-D) space. Partition vector incorporates other acceleration techniques to produce a method that reduces tracing time. The conventional verification of path loss and delay profiles predicted by ray tracing was extended to include the verification of angle of arrival (AOA). The results prove the necessity of extension and verify that path loss and delay profiles cannot fully confirm the accuracy of ray tracing in a spatial domain. A good level of accuracy was observed in the comparison of three key areas: (1) path loss, (2) delay profile, and (3) AOA. Degradation of prediction accuracy caused by incorrectly predicted phases in ray tracing was investigated, and improvements were made by incorporating a "random-phase" approach. It was found that measured path loss and delay profiles are almost fully confined within the 90% confidence interval, proving that the approach can account for the degradation effects caused by inaccurate antenna positions. The applicability of limited-band and limited beam width channel parameters transformed from ray-tracing results is also examined in the sense of an azimuth delay profile. The confirmation of the accuracy of the profile with measurement prepares ground for the use of ray-tracing approaches to analyze system performance in real environments.

1. Introduction

The recent growth in demand for multimedia services and higher data transmission speeds is dictating the nature of wireless communication systems. In the future such systems are likely to have the following characteristics: (1) multimedia communication to accommodate voice, data, and video services, (2) higher data transmission rates (e.g., 2–10 Mbits/s and beyond), and (3) higher frequency bands (e.g., 2–8 GHz).

The multipath propagation nature of wireless transmission channels can cause a number of problems for high-speed and microwave band wireless systems. These problems include (1) serious intersymbol interference (ISI) due to higher date rates, (2) serious propagation loss due to higher-frequency bands, and

Paper number 1999RS002202.
0048-6604/01/1999RS002202$11.00

(3) cochannel interference due to the reduction of the cell size.

The first of these problems is caused by a time domain impact of the channel. The others are due to space domain issues. The following techniques are proposed to address these effects: (1) adaptive equalizer, (2) interference cancellation, (3) smart (adaptive) antenna, and (4) spread spectrum (SS) and orthogonal frequency-division multiplexing (OFDM) modulation schemes. The prerequisite for the proper design and analysis of these techniques is an accurate radio channel model that incorporates the spatial and temporal characteristics of wireless channels [*Fleury and Leuthold,* 1996; *Ertel et al.,* 1998].

By incorporating site-specific information, ray-tracing methods predict detailed channel parameters such as complex channel impulse response characteristics. Nevertheless, current ray-tracing methods mainly focus on predicting path loss and calculating cell coverage [*Erceg et al.,* 1997; *Imai and Fujii,* 1997; *Athanasiadou et al.,* 1997, 1998; *Papadakis et al.,* 1998]. Furthermore, angle of arrival (AOA) information is difficult to extract from conventional measurement methods, and it is therefore difficult to verify ray-tracing results. In addition, a number of disadvantages inherent in existing ray-tracing methods frustrate people who use them. For example, although three-dimensional (3-D) ray-launching methods [*Seidel and Rappaport,* 1994] launch rays from an icosahedron, they are launched with unequal separating angles that can deteriorate the accuracy of a calculation. Although the capture circle [*Honcharenko et al.,* 1992] works perfectly in two dimensions, in three dimensions it has double-counting error problems that can result in a 3 dB error [*Durgin et al.,* 1997], caused by the incoherent accumulation of additional power. Alternatively, image methods [*Kanatas et al.,* 1997; *Rizk et al.,* 1997] normally require a substantial amount of memory to establish various order image sources. To reduce the computational complexity and improve accuracy, a 2-D/3-D hybrid ray-tracing method is proposed for the purpose of building a spatiotemporal channel model.

In this paper we use the proposed ray-tracing method to build and verify a spatiotemporal channel model that is expressed as a linear filter with a complex baseband impulse response that combines spatial information and polarization. Two-dimensional ray-tracing methods are described by *Erceg et al.* [1997] and *Liang and Bertoni* [1998]. However, the transformation from 2-D rays to 3-D ray paths has not been clearly defined. In the proposed ray-tracing method the authors try to accelerate the speed of ray tracing (section 3.1.2) and improve ray-tracing accuracy (sections 3.2.2 and 3.2.3). In addition, the authors attempt to verify the prediction accuracy of the ray-tracing method with respect to angles. These activities provide the confidence to extend the application of ray-tracing approaches to spatiotemporal channel modeling.

The organization of this paper is as follows: Section 2 provides the proposed spatiotemporal channel model formulation. The ray-tracing method and the detailed algorithm are presented in section 3. Section 4 describes the measurement and comparison of ray-tracing results with measurement data in three key areas: (1) path loss, (2) delay profile, and (3) AOA. Finally, section 5 draws conclusions on the verification of this ray-tracing method.

2. Spatiotemporal Channel Model

In this paper the spatiotemporal channel-modeling scheme is extended from *Turin et al.*'s [1972] statistical channel model. By incorporating spatial information (AOA) and polarization this model takes the form of a dyadic baseband complex impulse response as

$$\begin{aligned}\overline{\mathbf{H}}(t,\tau,\theta^t,\phi^t,\theta^r,\phi^r) &= \sum_{i=0}^{n}\left[\hat{\mathbf{\Theta}}_i^t \quad \hat{\mathbf{\Phi}}_i^t\right]\begin{bmatrix} A_i^{\theta\theta} & A_i^{\theta\phi} \\ A_i^{\phi\theta} & A_i^{\phi\phi}\end{bmatrix}\begin{bmatrix}\hat{\mathbf{\Theta}}_i^r \\ \hat{\mathbf{\Phi}}_i^r\end{bmatrix} \\ &\cdot\delta(\theta^t-\theta_i^t)\delta(\phi^t-\phi_i^t)\delta(\theta^r-\theta_i^r)\delta(\phi^r-\phi_i^r) \\ &\cdot\delta(\tau-\tau_i)e^{j\psi_i}e^{-j\mathbf{k}_i\cdot\mathbf{v}t}, \end{aligned} \tag{1}$$

where all the parameters are shown as follows:

$A_i^{\theta\theta}, A_i^{\theta\phi}, A_i^{\phi\theta}, A_i^{\phi\phi}$	path gain;
τ_i	delay time;
$\hat{\mathbf{\Theta}}_i^t, \hat{\mathbf{\Phi}}_i^t$	transmitting angle vector;
$\hat{\mathbf{\Theta}}_i^r, \hat{\mathbf{\Phi}}_i^r$	receiving angle vector;
ψ_i	phase;
$\mathbf{k}_i\cdot\mathbf{v}t$	Doppler shift.

Doppler shift and polarization are not included in the verification because they are difficult to determine. In real applications, when the vector antenna pattern is given, a detailed channel response is obtained by integrating the product of the vector antenna pattern with (1). As for the uniform linear array antennas, the detailed response of each element is obtained in a similar way except that each ray is added with an offset phase relative to the reference element.

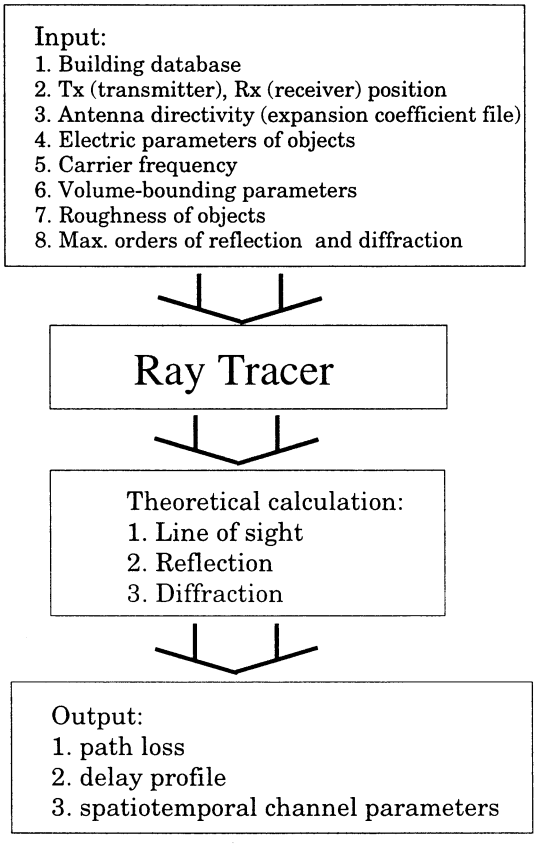

Figure 1. Block diagram of our ray-tracing tool.

3. Hybrid Ray-Tracing Method

The purpose of the proposed ray-tracing tool is the prediction of spatiotemporal channel parameters in microcellular and picocellular environments. The following assumptions are made: (1) Transmitting antenna heights are below the rooftops of surrounding buildings. (2) The ground is smooth and flat. (3) Walls of buildings are perpendicular to the ground.

The main body of the proposed 2-D/3-D hybrid ray-tracing method can be divided into two parts: (1) ray tracing and (2) electromagnetic wave calculation (Figure 1). Ray tracing traces rays from transmitter to receiver as efficiently as possible to find detailed ray paths. Electromagnetic wave calculation uses electromagnetic wave theory (such as the uniform theory of diffraction (UTD)) to calculate theoretical values in a realistic environment.

3.1. Ray-Tracing Formulation

The 2-D/3-D hybrid ray-tracing method is based on the ray-launching idea proposed by *Seidel and Rappaport* [1994], which regards the transmitter as being a point source that launches rays in every direction. In the proposed approach, rays are launched in a two-dimensional horizontal plane with equal angle separation. The location of the reflection and diffraction points and the formulation of reflected and diffracted rays are carried out based on geometrical optics (GO), Snell's law of reflection, and Keller's law of diffraction [*Keller,* 1962].

3.1.1. Determination of the ray path. When vertical walls are only considered, 2-D tracing gives correct 3-D results. The locations of reflection points are determined by simple line and line intersection in a two-dimensional coordinate system. Since the incident angle should be equal to the reflection angle (the law of reflection), the reflected ray vector is determined by the following simple vector calculation [*Glassner,* 1989]:

$$\hat{\mathbf{k}}_r = \hat{\mathbf{k}}_i - 2\,(\hat{\mathbf{n}}\cdot\hat{\mathbf{k}}_i)\,\hat{\mathbf{n}}, \tag{2}$$

where $\hat{\mathbf{k}}_i$ is the unit vector of the incident ray, $\hat{\mathbf{n}}$ is the unit vector of the surface normal, and $\hat{\mathbf{k}}_r$ is the unit vector of the reflected ray.

Building corners are checked by setting up capture circles to determine diffraction points [*Honcharenko et al.,* 1992]. As the incident angle (the angle between the incident ray and the edge of a building wall) is equal to the diffraction angle (the angle between the diffracted ray and the edge of a building wall), if we virtually unfold the incident plane and diffraction plane into one plane (as shown in Figure 2), the incident ray and the diffracted ray are actually in a straight line. After determining the intersection points (see Figure 2) the ray paths are established by geometrically calculating the heights of intersection points. The height h_k of the kth reflection or diffraction point is obtained as

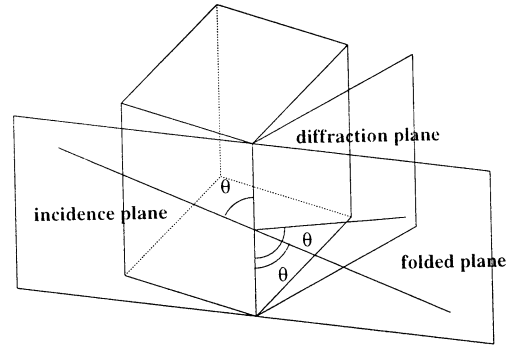

Figure 2. Illustration of Keller's law of diffraction.

$$h_k = \frac{L_{tk}h_r + h_t(L_{tr} - L_{tk})}{L_{tr}}, \quad (3)$$

where L_{tk} is a 2-D ray path length from the transmitter to the intersection point, L_{tr} is a 2D ray path length from the transmitter to the receiver, h_t is the height of the transmitter and h_r is the height of the receiver.

As each ray path generates a pair of rays (one with ground reflection and one without), ground-reflected rays are formed by searching the ground reflection point in the previous ray path. The ray path length from the transmitter to the ground reflection point L_{tg} is calculated by

$$L_{tg} = \frac{h_t L_{tr}}{h_t + h_r}. \quad (4)$$

The ground reflection point is formed along the ray path, and the heights of other intersection points are adjusted by (3). Finally, the heights of intersection points are compared with the heights of the buildings. If one of the intersection points is higher than the building, the ray path does not exist.

The capture circle [*Honcharenko et al.*, 1992] is set up to determine whether the ray reaches each building corner and receiving point or not. The circle radius is defined as $0.5\alpha L$, where α is the angle separation and L is the whole length of the ray path between the source and the capture circle. Although calculation accuracy is improved when launching angle separation is smaller, computational time increases. There is a trade-off between accuracy and computational time with regard to launching angle separation. In the authors' experiences a 0.1°—1° launching angle separation is sufficient for picocells (0.1°—0.5° for 60 × 60 m^2) and microcells (0.5°— 1° for 600 × 600 m^2). In addition to the ray reaching the receiving point, ray tracing is terminated if one of the following three conditions is met: (1) the signal level of the ray is below the threshold value, (2) the intersection order of the ray exceeds the user-specified maximum reflection and diffraction order, or (3) the ray leaves the whole area.

In order to save computational time the order of reflections is limited up to 20, and the maximum order of diffractions is limited up to 2 (referring to other ray-tracing tools [*Athanasiadou et al.*, 1998].

3.1.2. Application of ray acceleration techniques. To decrease computational time, a series of ray acceleration techniques [*Foley et al.*, 1997] is used in the proposed ray-tracing tool.

3.1.2.1. Back-face culling: This technique can be seen in Figure 3. Since most computational time is spent on intersection checks, the authors' main intention is to reduce intersection check times. The dot product of the normal vector of a surface (building wall) and the launching ray vector is used to determine if the wall is invisible to the launching ray (back face). If the dot product is greater than zero, the building face is invisible to the launching ray and it does not need to be checked for an intersection.

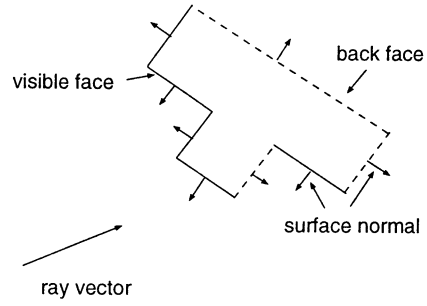

Figure 3. Illustration of the back-face culling idea.

3.1.2.2. Volume bounding: This technique is used to reduce the number of buildings required for an intersection check [*Cátedra et al.*, 1998]. An area is divided into several rectangular subareas (bounding volume), and users specify the size of the bounding volume. When the bounding volume intersected by the ray is determined, the buildings in that volume are checked for an intersection. Without this technique every building in the area would have to be checked. Thus computational time would be dramatically increased.

3.1.2.3. Partition vector: The authors propose partition vector (PV) as a simple but effective technique for ray acceleration. The ray vector is bound with two partition vectors: unit vectors that start from the endpoint of the current ray vector and can have positive/negative x- or y-axis direction. A bounding area formed by using two partition vectors in one bounding volume is shown in Figure 4. If the coordinates of one of the buildings' corners are confined in the bounding area, this building then qualifies for an intersection check.

3.2. Theoretical Calculation

The proposed ray-tracing tool allows the user to specify the positions of the transmitter and the receiver, the electrical parameters (conductivity and permittivity) of every building and ground plane, and carrier frequency and the vector field directivity of antennas. Since, in real environments, building

walls may not be smooth, the roughness of reflecting surfaces can be specified by the standard deviation of the surface height with respect to the mean surface height. The randomness of the surface height is assumed to be modeled by a Gaussian distribution.

3.2.1. Field calculation. The rotation of the polarization vector is considered for each reflection and diffraction event. The dyadic reflection and diffraction coefficients [*Balanis,* 1989] are used for the field calculation. At reflection and diffraction points the electric field components in the global coordinate system $E_{x,y,z}$ are first resolved into parallel and perpendicular components (with respect to the incidence plane) and multiplied by corresponding reflection/diffraction coefficients. After the calculation the polarization components are resolved again to $E_{x,y,z}$ in the global Cartesian coordinate system. The average rough surface reflection coefficient [*Landron et al.,* 1996] and the heuristic dielectric wedge diffraction coefficient [*Luebbers,* 1984] from UTD are used for the calculation of reflection and diffraction loss.

The received electric field at the receiving antenna is therefore calculated by the following formulas:
Direct ray

$$\mathbf{E}_{\mathrm{LOS}} = \frac{\mathbf{E}_0}{d} e^{-jkd}, \tag{5}$$

Reflected rays

$$\mathbf{E}_{\mathrm{R}} = \frac{\mathbf{E}_0}{d} \cdot \overline{\mathbf{R}}_{\mathrm{rough}} e^{-jkd}, \tag{6}$$

Once-diffracted rays

$$\mathbf{E}_{\mathrm{D}} = \frac{\mathbf{E}_0}{s'} \cdot \overline{\mathbf{R}}_{\mathrm{rough}} \cdot \overline{\mathbf{D}} \cdot \sqrt{\frac{s'}{s(s'+s)}} e^{-jk(s+s')}, \tag{7}$$

Twice-diffracted rays [*Erceg et al.,* 1997]

$$\mathbf{E}_{\mathrm{DD}} = \frac{\mathbf{E}_0}{s'} \cdot \overline{\mathbf{R}}_{\mathrm{rough}} \cdot \overline{\mathbf{D}}_1 \cdot \overline{\mathbf{D}}_2 \cdot \sqrt{\frac{s'}{ss''(s'+s+s'')}} e^{-jk(s+s'+s'')}, \tag{8}$$

where $\mathbf{E}_0$ is the emitted electric field observed at the unit distance, d is a propagation path length, s' is the path length from the source to the first diffracting wedge, s is the path length from the first diffracting wedge to the receiver (for once-diffracted rays) or to the second diffracting wedge (for twice-diffracted rays), s'' is the path length from the second diffracting wedge to the receiver, $\overline{\mathbf{R}}_{\mathrm{rough}}$ is a dyadic reflection coefficient of the rough surface, and $\overline{\mathbf{D}}$ is a dyadic diffraction coefficient of the dielectric wedge.

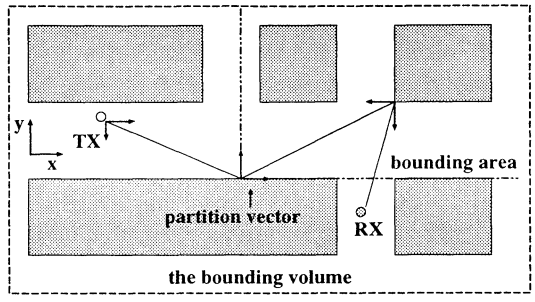

Figure 4. Application of partition vectors in one bounding volume.

The total field strength at any receiving point is contributed by reflected, diffracted, and multiple-reflected/multiple-diffracted signals due to the multipath phenomena. This is calculated by the deterministic linear superposition of all single contributions. Incorporating the antenna directivities (described in section. 3.2.2), it is expressed as follows:

$$E_{\mathrm{total}} = \sum_{i=1}^{k} A_i e^{j\phi_i}. \tag{9}$$

While assuming an infinitesimally small dipole antenna along $\hat{\mathbf{l}}$ at the receiving point, E_{total} is simply expressed as

$$E^{\hat{\mathbf{l}}}_{\mathrm{total}} = (\sum_{i=1}^{k} A_i e^{j\phi_i} \hat{\mathbf{e}}_i) \cdot \hat{\mathbf{l}}, \tag{10}$$

where A_i is the amplitude of the ith arrival ray ($|E_i|$), ϕ_i is the phase of the ith arrival ray, $\hat{\mathbf{l}}$ is a unit vector of direction, $\hat{\mathbf{e}}_i$ is a unit vector of polarization of the ith arrival ray.

Here ϕ_i is given as follows:

$$\phi_i = \psi_i - kd_i, \tag{11}$$

where ψ_i is the phase shift caused by interaction with obstacles and d_i is the propagation path length of the ith arrival ray.

In fact, normal ray-tracing methods cannot predict phase ϕ_i correctly because of inaccurate antenna positions and building databases. In the proposed approach, ϕ_i is assumed to be random. A statistical superposition of single contributions to calculate the total field strength is therefore adopted (as described in section 3.2.3).

3.2.2. Calculation of the vector antenna pattern. Normally, the antenna radiation pattern used in ray tracing is approximated by the **E** and **H** plane pattern [*Hammoudeh et al.,* 1999] or applied by a 3-D radiation pattern stored in the computer [*Athanasiadou et al.* 1997]. The former may not be particularly accurate since the antenna emits rays in 3-D. The latter wastes computer memory. In the proposed approach, far-field pattern functions $\mathbf{K}_{smn}(\theta,\phi)$ and the expansion coefficient Q_{smn} [*Hansen,* 1988] express the field directivity pattern of the antenna. The index s distinguishes the two modes: The $s = 1$ denotes transverse electric (TE) mode, and $s = 2$ denotes transverse magnetic (TM) mode. The indices m and n indicate the mode numbers of the wave functions in the ϕ and θ directions, respectively.

Since the radiating power of the antenna is given by

$$P = 1/2\sum_{smn}|Q_{smn}|^2, \tag{12}$$

the transmitting power can be normalized to a 0 dB gain, and the vector directivity function is obtained as

$$\mathbf{D}(\theta,\phi) = \frac{\sum_{smn} Q_{smn}\mathbf{K}_{smn}(\theta,\phi)}{\sqrt{\sum_{smn}|Q_{smn}|^2}}. \tag{13}$$

Therefore, if the field pattern of any antenna is given, the expansion coefficient is obtained by the following equation:

$$Q_{smn} = \oint_{\Omega} \mathbf{E}\cdot\mathbf{K}^*_{smn}d\Omega. \tag{14}$$

The expansion coefficient is stored as a lookup table in the computer. Finally, the emitted field is calculated according to (13) and resolved into $E_{x,y,z}$ components from spherical coordinates in the global coordinate system. The use of the far-field pattern function has some advantages. First, it strictly satisfies Maxwell's equations and is therefore widely used in spherical near-field antenna measurements [*Hansen,* 1988]. Second, the mode number of the function, sufficient to the expansion, is limited and proportional to the antenna size. This can reduce the need for computer memory to store antenna patterns.

3.2.3. Application of the random phase approach. The conventional power-summing approach [*Erceg et al.,* 1994] sums up the power of each individual ray to obtain the total signal level by assuming that the incoming rays are incoherent. However, this approach cannot indicate the fluctuation range of the signal level or demonstrate the fading phenomena. Alternatively, the phase-summing approach [*Erceg et al.,* 1994] calculates the total signal level from the sum of individual complex rays. Fast variation (multipath fading) of the signal can be observed in the total signal level. However, the calculation is quite possibly corrupted by the phase errors of some rays. This approach also requires a sufficiently large averaging window to obtain the spatial average of the signal [*Erceg et al.,* 1994]. This large averaging window is not appropriate to microcell and picocell environments. In the proposed approach, the idea of random phase ray tracing [*Takahashi et al.,* 1998] is adopted to model the level of fluctuation due to the coherent interaction among different rays.

Since the building database and the positions of the antennas may not be accurate on the order of wavelength, a phase error is introduced into each ray. This may dramatically deteriorate the accuracy of the ray-tracing results. As the total field at the receiving point is expressed in (9), phase ϕ_i is therefore assumed to be random. The cumulative probability of the total field strength (fading statistics) at the receiving point can be derived by the characteristic function method [*Takahashi et al.,* 1998] and is given as [*Barakat,* 1974]

$$P(|E|) = \frac{2|E|}{R}\sum_{n=1}^{\infty}\frac{\Phi(\gamma_n/R)}{\gamma_n J_1^2(\gamma_n)}J_1\left(\frac{\gamma_n|E|}{R}\right), \tag{15a}$$

where γ_n is the nth root of zeroth-order Bessel function $J_0(\ )$, $J_1(\ )$ is the first-order Bessel function, and

$$\Phi(x) = \exp\left(-\frac{\sigma^2x^2}{2}\right)\prod_{i=1}^{k}J_0(A_ix), \tag{15b}$$

where σ^2 is the receiver noise power, A_i is the am-

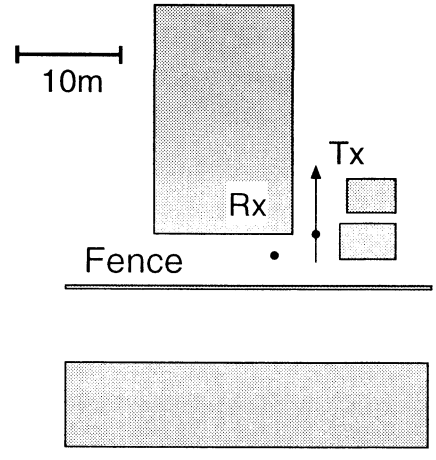

Figure 5. A picocell measurement environment at TIT.

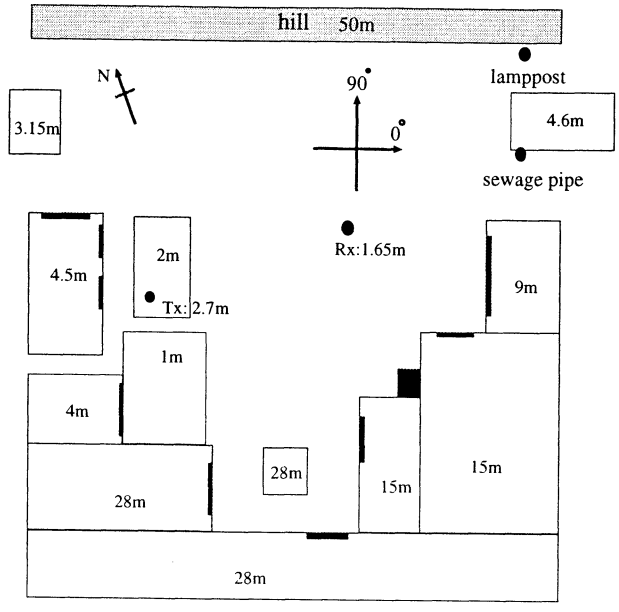

Figure 6. A picocell measurement environment in YRP.

plitude of the ith ray, and R is an upper limit parameter, as sufficiently large as possible and chosen as [*Jao and Elbaum*, 1978]

$$R = \sum_{i=1}^{k} A_i + 5\sigma. \tag{15c}$$

The total field strength corresponding to the cumulative probability from 5 to 95% is selected as the confidence interval. If the measured data are confined within the confidence interval, it implies that the ray-tracing tool gives the correct predictions. The prediction error of ray-tracing approaches, caused by incorrect phases, can also be improved by using the local mean calculated by the random phase approach. By incorporating the random phase approach into the ray-tracing method it provides an insight into the fading mechanism and also a specific range within which the signal level will fluctuate.

Table 1. Electrical Parameters Used in Ray Tracing

	ϵ_r	σ, S/m
Building wall	5.5	0.023
Ground plane	15.0	0.005
Metal	-	∞
Hill	3.5	0.01

4. Field Measurement and Comparison

In this section, we describe three field measurements. The first was carried out inside the campus of the Tokyo Institute of Technology (TIT), the second was carried out in Yokosuka Research Park (YRP), and the third was carried out in Yokosuka Highland. The first two measuring environments are shown in Figures 5 and 6. Both measurement sites are typical picocell cases with areas under 60×60 m^2. Since it is very difficult to verify the calculation accuracy of ray tracing in AOA, a good starting point is to compare ray-tracing results with measurement in picocell environments. The TIT measurement environment is rather simple, and the YRP measurement environment is quite complex, with mixed heights of buildings and a nearby hill. A metal pillar and doors are indicated by a wide solid rectangle and thin solid rectangles, respectively. The heights of a car, buildings, and antennas are also shown in Figure 6. Fur-

Table 2. Simulation Parameters Used in Ray Tracing

	TIT	YRP	Yokosuka
Carrier frequency, Hz	1.28 G	8.45 G	3.35 G
Transmitter height, m	1.45	2.7	4.0
Receiver height, m	1.45	1.65	2.7
Reflection order	4	6	4
Diffraction order	1	1	2
Antenna	vertically polarized half-wave dipole		

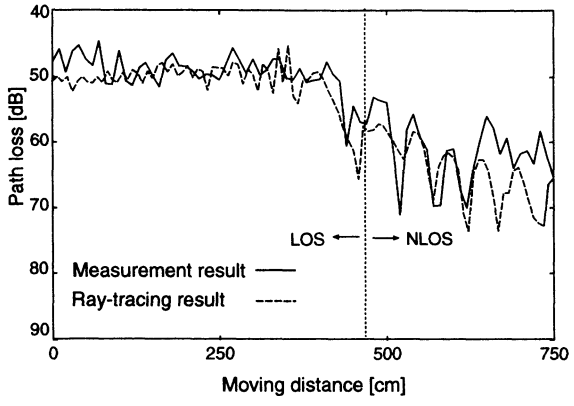

Figure 7. Path loss variation indicating short-term fading effect.

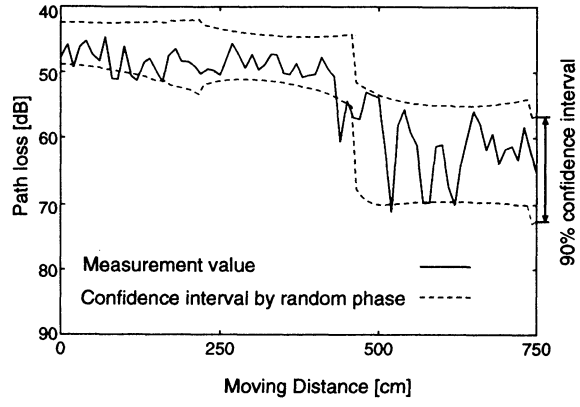

Figure 9. Measurement result compared with random phase ray-tracing result.

thermore, to confirm the accuracy of the proposed ray-tracing tool in microcell environments, the authors also compared the path loss result with published measurement data in a microcell environment of Yokosuka Highland. The electrical parameters [*International Radio Consultative Committee (CCIR),* 1991] used for the calculation of ray tracing in all environments are listed in Table 1. The other simulation parameters are listed in Table 2. By increasing the order of reflections and diffractions in these environments the results did not change considerably. The measurements of path loss, delay profile, and AOA were carried out and compared with the ray-tracing results.

4.1. Path Loss

As to path loss, measurement in both a microcell and a picocell are compared with ray-tracing results.

4.1.1. TIT measurement. During the TIT measurement (picocell) the transmitter moved from the line-of-sight (LOS) area to the non-LOS (NLOS) area while the receiver was put in a fixed position. The transmitter antenna was connected to a signal generator, and 1.28 GHz CW of 10 dBm was transmitted. A spectrum analyzer measured the received signal level. The whole moving range was 7.5 m, and the transmitter moved at a step of 10 cm, which was nearly equal to 0.5λ of the CW.

Figure 7 shows the measured path loss together with the ray-tracing result by phase summing. Figure 8 shows a local mean calculated over 1 m range with the moving-average method for comparison. Even though agreement can be observed between the measurement and the ray-tracing result, a difference is observed in the NLOS region. However, using the random phase ray-tracing method described in section 3.2.3, a 90% confidence interval of the path loss is calculated (see Figure 9). Almost all of the measurement data fell into the 90% confidence interval.

This result implies that the averaging effect of the moving-average method applied in processing the

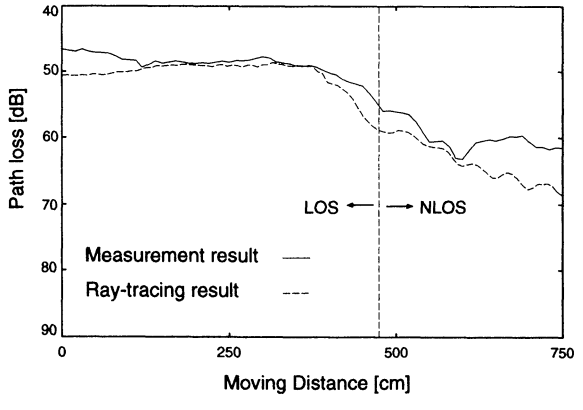

Figure 8. Path loss variation after averaging.

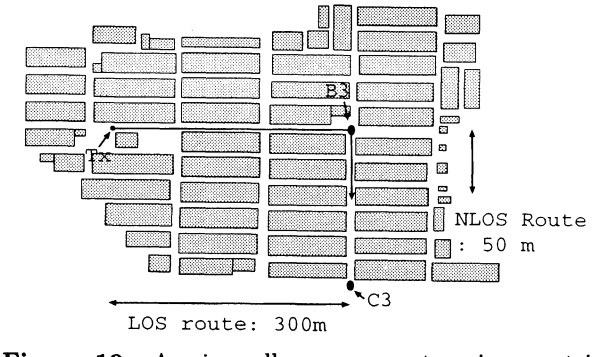

Figure 10. A microcell measurement environment in Yokosuka city.

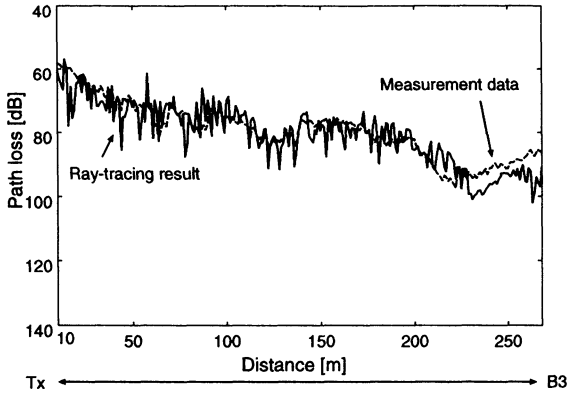

Figure 11. YRP measurement result of a LOS route compared with ray-tracing result.

ray-tracing result may not be enough to obtain the correct local mean as measurement. This is due to the limited averaging length. The accuracy of the local mean depends on the averaging length, which should be sufficiently large to include all combinations of the signal level fluctuation due to the phase rotation of arrival rays [*Takahashi et al.*, 1998]. However, in many cases this huge averaging length may not be practically possible. Moreover, even if the averaging length is large enough, the arrival rays will become different when the position of the receiving point changes. Thus the averaged mean may not be correct. This result shows that when compared with the random phase method, the moving-average approach may not give statistically correct channel parameters.

4.1.2. Yokosuka Highland measurement. A microcell measurement [*Shimizu et al.*, 1999] was done in a suburban part (600×600 m^2) of Yokosuka Highland (shown in Figure 10). The environment consists of buildings with an average height of 8 m. Several measuring routes were chosen during the measurement [*Shimizu et al.*, 1999]. As seen in Figure 10, a LOS measuring route ($\sim$ 300 m long) and a NLOS measuring route ($\sim$ 50 m long) are selected in this paper for comparison.

Seen from Figures 11 and 12, although there is some deviation observed at around 250 m in the LOS route, the good agreement between ray-tracing results and measurement can be seen in these graphs. The deviation of path loss between measurement and ray-tracing results is summarized in Table 3.

4.2. Delay Profile

4.2.1. TIT measurement. In TIT measurement the delay profile at a receiving point is measured by using a network analyzer [*Okada et al.*, 1998] which measures the transfer function at discrete frequency points. The inverse discrete Fourier transform (IDFT) is employed to get the band-limited impulse response, i.e., the delay profile. The sampled data are multiplied by a Hanning window function before using the IDFT. The measuring route and the moving step are the same as in section 4.1.1. The measuring frequency is centered at 1.28 GHz with a 200 MHz bandwidth. In this bandwidth the sampling frequency is separated by 1 MHz. At each receiving point we took 100 snapshots. The signal-to-noise ratio (SNR) is 25 dB in the LOS area and 15 dB in the NLOS area.

Since the delay profile from ray tracing is band-unlimited, the impulse response obtained by ray tracing was first transformed into the frequency domain and then limited by the bandwidth used in the measurement. Finally, the data were transformed into the time domain by the inverse Fourier transform. The random phase concept was also used to get the 90% confidence interval of the continuous-time delay profile.

The delay profile at the receiving point shown in Figure 5 is presented in Figure 13. The ray-tracing result was processed by adding each arrival ray with a random phase and then band-limited by 200 MHz to get the continuous-time plot form. The measured delay profile was found to be within the 90% confidence interval.

4.2.2. YRP measurement. A delay profile measurement system utilizing pseudonoise (PN) code [*Masui et al.*, 1999] is used here. A 8.45 GHz spread spectrum signal with 50 megachips/s data rate was transmitted. The whole dynamic range is above 60

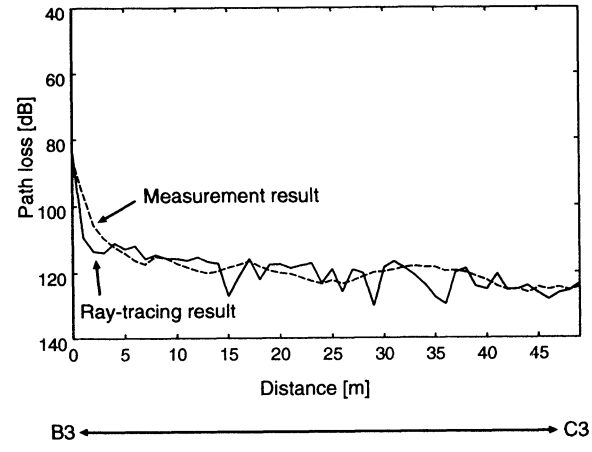

Figure 12. YRP measurement result of a NLOS route compared with ray-tracing result.

Table 3. Deviation of Path Loss Between Measurement and Ray-Tracing Results

	Mean, dB	Root-Mean-Square (RMS), dB
TIT (picocell)	1.43	1.57
Yokosuka (microcell)	0.99	4.76

dB (2047 chips of PN length), and the whole bandwidth of this system is 100 MHz [*Masui et al.*, 1999]. The receiving antenna is moved at 8×8 grid points with a 0.4λ separation distance between grids. Since the scattering effects of a small hill near the receiving point cannot be neglected, it is modeled as a tall rectangular obstacle. The effects of metal doors and pillars are also considered in the ray-tracing process.

The delay profiles corresponding to 5, 50 and 95% cumulative probabilities from all 64 delay profiles are extracted and plotted in Figure 14. Alternatively, the delay profiles corresponding to 5, 50 and 95% cumulative probabilities derived from the random phase approach are then compared with measurement results. Figure 15 shows the high level of agreement between the median delay profiles of ray tracing and measurement. Especially, there is an almost 100% overlap of the peaks of direct wave, second arrival waves, and third arrival waves in the graph. The overestimation of ray tracing is observed at around 260 ns. This may be caused by inaccurate approximation of electrical parameters or inaccurate phase summing. Figure 16 shows that the measured delay profiles with 5, 50, and 95% cumulative probabilities are almost totally confined within the 90% confidence interval calculated by the random phase approach. It proves that the random phase approach can provide an accurate varied range of delay profiles caused by inaccurate antenna positions (4λ in this case). This may provide confidence in predicting delay profiles with ray tracing.

4.3. Angle of Arrival

4.3.1. TIT measurement. In TIT measurement the AOA testing was implemented by moving a receiving antenna at 7×7 grid points with a 0.5λ separation distance. The measurement data were again obtained by the network analyzer and processed by 2-D Unitary ESPRIT algorithm to get both azimuth and elevation angles [*Zoltowski et al.*, 1996; *Sakaguchi et al.*, 1998]. The forward and backward smoothing was done 18 times by using a 5×5 subarray. The primary signal-to-noise ratio after ESPRIT processing was around 30 dB, and the 200 snapshots were taken. The heights of the transmitter and the receiver were set at 1.485 m. As seen in Figures 17 and 18, the AOAs of the direct wave, diffraction waves from two corners, and a reflection wave from the wall of the measurement data are in good agreement with the ray-tracing result.

4.3.2. YRP measurement. The AOA measurement in YRP is quite similar to that at TIT. The measuring system and the transmitter and receiver settings are the same as those used in the measure-

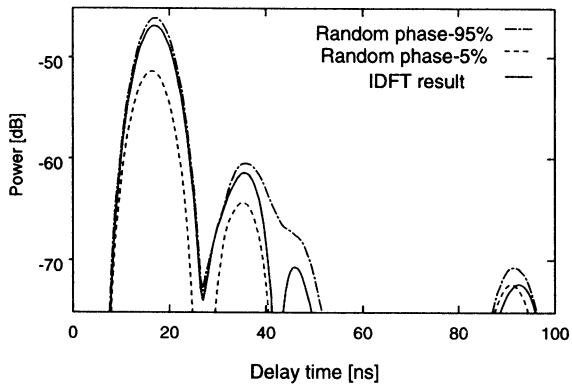

Figure 13. A delay profile by IDFT and ray tracing.

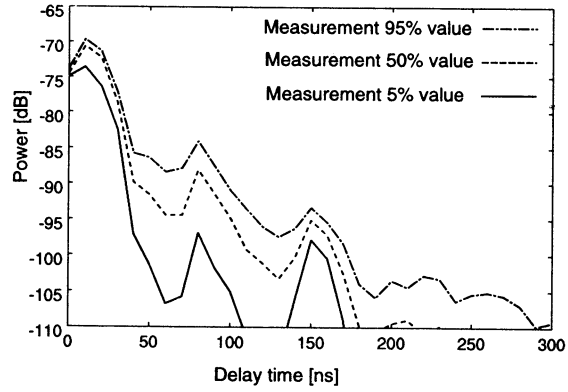

Figure 14. Measured delay profiles in YRP measurement.

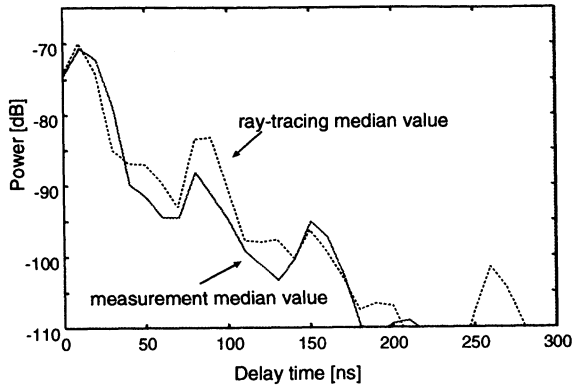

Figure 15. Comparison of median delay profiles in YRP measurement.

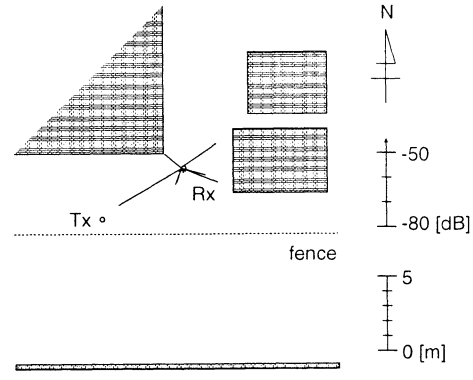

Figure 17. Spatial channel parameters predicted by ray tracing.

ment of the delay profile. The receiving antenna is moved at 8×8 grid points with a 0.4λ separation distance of grids. A 8×8 two-dimensional array antenna system is therefore simulated. An azimuth delay power profile (beam-forming pattern) of this antenna system is calculated and compared with the corresponding ray-tracing result. The ray-tracing result is first transformed into the band-limited response in delay domain and then multiplied with a weight vector (rotate in azimuth degrees) of this array antenna to generate the beam-forming pattern.

These azimuth delay beam-forming patterns are projected into the azimuth plane. Figure 19 shows the projection of the ray-tracing result. Figure 20 plots the projection of measurement data and the arrival rays calculated by ray tracing. From these comparisons, good agreement can be observed at the direct wave (at around 200°) and some scattered waves (at 80°, 240°, and 350°). However, the arrival waves between 40° and 80° are not predicted by ray tracing. Actually, there is a metal lamppost and a metal sewage pipe almost at these directions (as seen in Figure 6). This could be the reason for these arrival waves because the lamppost and the sewage pipe are not modeled in the ray tracing. Therefore it may be necessary to model some obstacles such as lampposts in ray tracing, especially for high-frequency systems (8.45 GHz) in picocell environments. This implication may not be evident if using the conventional comparison in path loss and delay profile.

Figures 21 and 22 show the azimuth delay power profiles of measurement and ray tracing, respectively. The observation of these graphs also proves the good calculation accuracy of the proposed ray-tracing tool. It is noted that there is a small angular difference if the results are carefully compared (as seen in Figure 20). For example, although the peak of direct

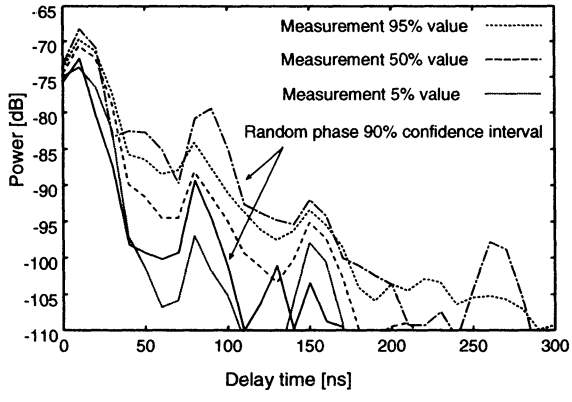

Figure 16. Illustration of measured delay profiles confined within the 90% confidence interval calculated from the random phase approach in YRP measurement.

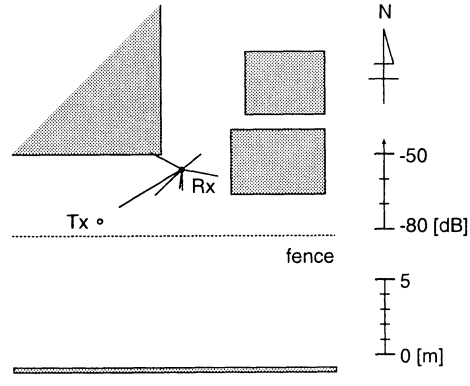

Figure 18. Spatial channel parameters measured and processed by ESPRIT.

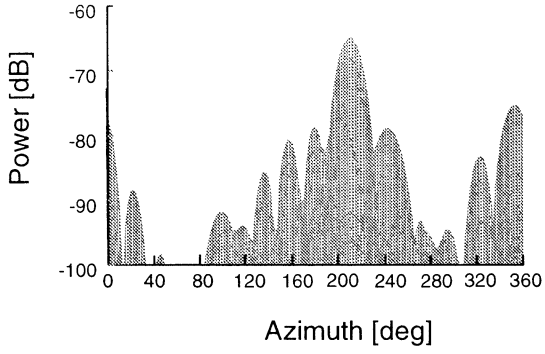

Figure 19. Projection of an azimuth delay profile from ray tracing into the azimuth plane.

wave is almost perfectly predicted, the peaks of reflected waves at 350° show a $\sim 5°$ difference which is probably caused by a small coordinate error of antenna positions. Overall, the proposed ray-tracing tool showed a good level of accuracy and was fully verified with regard to the path loss, the delay profiles, and the angle of arrival.

4.4. Spatiotemporal Channel Modeling

In a conventional ray-tracing process the received rays have unlimited frequency bandwidth and infinitely narrow beam width. The calculated spatiotemporal power profile is therefore a spatiotemporal channel impulse response without normalization. For example, the spatial and temporal channel parameters of the receiving point in Figure 17 can be graphically represented in Figure 23. Figure 23 indicates that the ray-tracing method may be quite suitable for the formulation of the spatiotemporal channel model. However, because of the site-specific nature of ray-tracing processes, such modeling loses generality and abstractness of mobile channels.

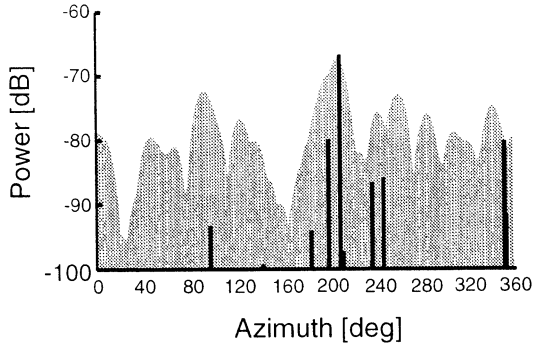

Figure 20. Comparison of AOA in the azimuth plane.

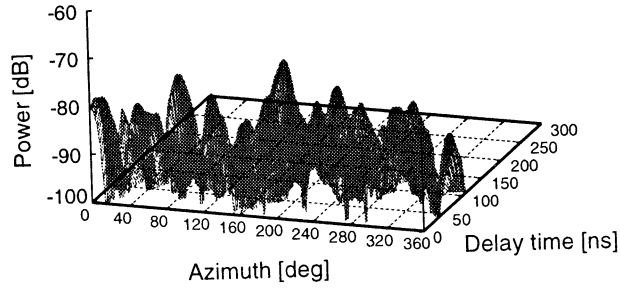

Figure 21. An azimuth delay profile obtained from measurement.

It is therefore not very appropriate for evaluation of channel transmission characteristics, which is normally based on a general (statistical) channel model. The exaction of a general channel model from ray-tracing processes may be an interesting area and will be continued in the future. Alternatively, the application of ray-tracing methods into direct assessment of system performance in a real environment is quite possible. In this assessment the results of a conventional ray-tracing process are required to have band-limited and finite-narrow beam width characteristics. In this sense, the proposed ray-tracing tool demonstrates the applicability and accuracy of this transformation in the comparison of Figures 21 and 22. This provides confidence in applying ray-tracing approaches to analyze system performance in both spatial and temporal areas.

5. Conclusion

This paper described a 2-D/3-D hybrid ray-tracing method for spatiotemporal channel modeling. A spatiotemporal channel model is proposed as a complex baseband impulse response by incorporating the spatial information and polarization. The efforts of this research were put on the acceleration of a ray-tracing process and the improvement of calculation accuracy. Partition vector is proposed as an effective ray-

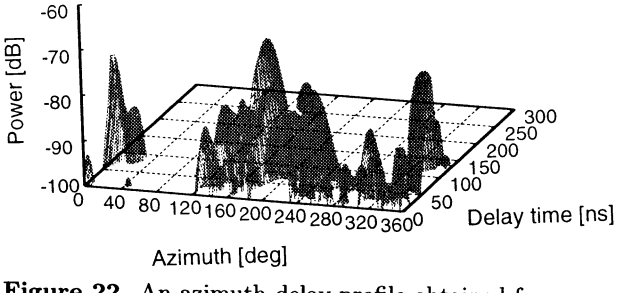

Figure 22. An azimuth delay profile obtained from ray tracing.

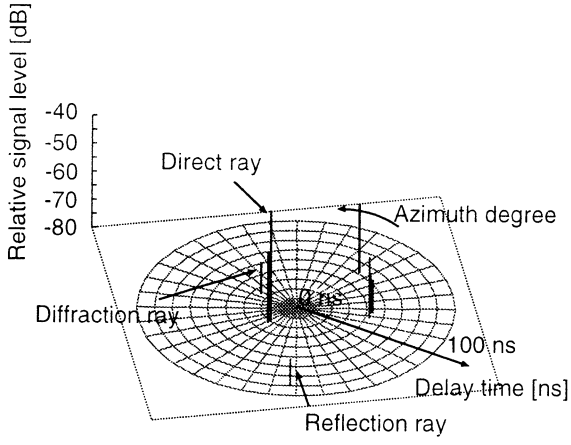

Figure 23. Spatiotemporal channel parameters.

tracing acceleration technique. The random phase approach is applied in ray tracing to give statistically correct results in the calculation of path loss and delay profiles. In addition, we also attempt to verify the prediction accuracy of the ray-tracing method with respect to angles.

Ray-tracing results have been compared with several measurements in picocell and microcell environments. The accuracy of the proposed ray-tracing tool was verified by the measurement data in three key areas: path loss, delay profile, and AOA. The comparison of path loss results suggests that it is more applicable to remove the fast-fading effects in ray-tracing results by using the random phase approach. It is also found that the random phase approach provides an effective approach to model the effects caused by inaccurate antenna positions. The good prediction accuracy of AOA by ray tracing in picocell environments is also proved by measurement. It is found that the effects of scattering obstacles such as lampposts cannot be neglected in ray tracing in picocell environments. The applicability of transformation from unlimited-band and infinitely narrow beam width ray-tracing results to limited-band and limited beam width channel parameters is also investigated and proved to be effective. This provides the confidence of applying ray-tracing approaches in analysis of the performance of specific systems in real environments.

Acknowledgments. The authors would also like to thank N. Abe, N. Sakai, T. Okada, and K. Sakaguchi of Tokyo Institute of Technology and H. Masui, H. Shimizu, M. Ishii, and K. Sakawa of YRP Key Technology Laboratories for their cooperation and help in the experiments. This work is partly supported by the Scientific Grant in Aid from Japanese Ministry of Education.

References

Athanasiadou, G., A. Nix, and J. McGeehan, Comparison of predictions from a ray tracing microcellular model with narrowband measurements, paper presented at 47th IEEE Vehicular Technology Conference, Inst. of Electr. and Electron. Eng., Phoenix, Ariz., May 4–7, 1997.

Athanasiadou, G., A. Nix, and J. McGeehan, Investigation into the sensitivity of a microcellular ray-tracing model and comparison of the predictions with narrowband measurements, paper presented at 48th IEEE Vehicular Technology Conference, Inst. of Electr. and Electron. Eng., Ottawa, May 18–21, 1998.

Balanis, C., *Advanced Engineering Electromagnetics*, John Wiley, New York, 1989.

Barakat, R., First-order statistics of combined random sinusoidal waves with applications to laser speckle patterns, *Opt. Acta, 21*(11), 903–921, 1974.

Cátedra, M., J. Pérez, F. Saez de Adana, and O. Gutierrez, Efficient ray-tracing techniques for three-dimensional analyses of propagation in mobile communications: Application to picocell and microcell scenarios, *IEEE Antennas Propag. Mag., 40*(2), 15–27, 1998.

Durgin, G., N. Patwari, and T.S. Rappaport, An advanced 3D ray launching method for wireless propagation prediction, paper presented at 47th IEEE Vehicular Technology Conference, Inst. of Electr. and Electrono. Eng., Phoenix, Ariz., May 4–7, 1997.

Erceg, V., A. J. Rustako Jr., and R. S. Roman, Diffraction around corners and its effects on the microcell coverage area in urban and suburban environments at 900 MHz, 2 GHz, and 6 GHz, *IEEE Trans. Veh. Technol., 43*(3), 762–766, 1994.

Erceg, V., S. J. Fortune, J. Ling, A. J. Rustako Jr., and R. A. Valenzuela, Comparisons of a computer-based propagation prediction tool with experimental data collected in urban microcellular environments, *IEEE J. Selec. Areas Commun., 15*(4), 677–684, 1997.

Ertel, R. B., P. Cardieri, K. W. Sowerby, T. S. Rappaport and J. H. Reed, Overview of spatial channel models for antenna array communication systems, *IEEE Personal Commun., 5*(1), 10–22, 1998.

Fleury, B. H., and P. E. Leuthold, Radiowave propagation in mobile communications: an overview of European research, *IEEE Comm. Mag., 34*(2), 70–81, 1996.

Foley, J. D., A. van Dam, S. K. Feiner, and J. F. Hughes, *Computer Graphics Principles and Practice*, pp. 660–663, Addison–Wesley-Longman, Reading, Mass., 1997.

Glassner, A. S., Surface physics for ray tracing, in *An Introduction to Ray Tracing*, edited by A. S. Glassner, pp. 131–133, Academic, San Diego, Calif., 1989.

Hansen, J. E., *Spherical Near-Field Antenna Measurements*, pp. 312-342, Inst. of Electr. Eng,, London, 1988.

Hammoudeh, A., M. Sánchez, and E. Grindrod, Experimental analysis of propagation at 62 GHz in suburban mobile radio microcells, *IEEE Trans. Veh. Technol., 48*(2), 576–587, 1999.

Honcharenko, W., H. L. Bertoni, J. L. Dailing, J. Qian, and H. D. Yee, Mechanisms governing UHF propaga-

tion on single floors in modern office buildings, *IEEE Trans. Veh. Technol., 41*(4), 496–504, 1992.

Imai, T., and T. Fujii, Propagation loss in multiple diffraction using ray tracing, paper presented at 1997 IEEE AP-S International Symposium, Inst. of Electr. and Electron. Eng. Antennas and Propag. Soc., Montreal, July 13–18, 1997.

International Radio Consultative Committee (CCIR), Electrical characteristics of the surface of the Earth, Recommendations and Reports of the CCIR, vol. V, Propagation in Non-Ionized Media, *Rec. 527-2,* Int. Telecommun. Union, Geneva, 1991.

Jao, J. K., and M. Elbaum, First-order statistics of a non-Rayleigh fading signal and its detection, *Proc. IEEE, 66*(7), 781–789, 1978.

Kanatas, A. G., I. D. Kountouris, G. B. Kostaras, and P. Constantinou, A UTD propagation model in urban microcellular environments, *IEEE Trans. Veh. Technol., 46*(1), 185–193, 1997.

Keller, J. B., Geometric theory of diffraction, *J. Opt. Soc. Am., 52*(2), 116–130, 1962.

Landron, O., M. J. Feuerstein, and T. S. Rappaport, A comparison of theoretical and empirical reflection coefficients for typical exterior wall surfaces in a mobile radio environment, *IEEE Trans. Antennas Propag., 44*(3), 341–351, 1996.

Liang, G., and H. Bertoni, A new approach to 3-D ray tracing for propagation prediction in cities, *IEEE Trans. Antennas Propag., 46*(6), 853–863, 1998.

Luebbers, R. J., Finite conductivity uniform GTD versus knife edge diffraction in prediction of propagation path loss, *IEEE Trans. Antennas Propag., 32*(1), 70–76, 1984.

Masui, H., K. Takahashi, S. Takahashi, K. Kage, and T. Kobayashi, Delay profile measurement system for microwave broadband transmission and analysis of delay characteristics in an urban environment, *IEICE Trans. Electron., E82-C*(7), 1287–1292, 1999.

Okada, T., K. Sakaguchi, N. Abe, J. Takada, and K. Araki, A comparative study of the delay profile measured by using ESPRIT algorithm and simulated by ray-tracing (in Japanese), paper presented at 1998 IEICE General Conference, Inst. of Electron., Inf., and Commun. Eng., Hiratsuka, Japan, March 27–30, 1998.

Papadakis, N., A. G. Kanatas, and P. Constantinou, Microcellular propagation measurements and simulation at 1.8 GHz in urban radio environment, *IEEE Trans. Veh. Technol., 47*(3), 1012–1026, 1998.

Rizk, K., J. Wagen, and F. Gardiol, Two-dimensional ray-tracing modeling for propagation prediction in microcellular environments, *IEEE Trans. Veh. Technol., 46*(2), 508–517, 1997.

Sakaguchi, K., J. Takada, and K. Araki, On measuring the delay profile and the directions of arrival by using super resolution algorithm, paper presented at 48th IEEE Vehicular Technology Conference, Inst. of Electr. and Electron. Eng., Ottawa, May 18–21, 1998.

Seidel, S. Y., and T. S. Rappaport, Site-specific propagation prediction for wireless in-building personal communication system design, *IEEE Trans. Veh. Technol., 43*(4), 879–891, 1994.

Shimizu, H., H. Masui, M. Ishii, K. Sakawa, and T. Kobayashi, LOS and NLOS path-loss and delay characteristics in microwave suburban propagation (in Japanese), paper presented at 437th URSI-F seminar, Int. Union. Radio Sci. Commission F, Yokosuka, Japan, Sept. 17, 1999.

Takahashi, S., Y. Yamada, and K. Ogura, Propagation-loss prediction using ray tracing with a random-phase technique, *IEICE Trans. Fundam., E81-A*(7), 855–859, 1998.

Turin, G., F. Clapp, T. Johnston, S. Fine, and D. Lavry, A statistical model of urban multipath propagation, *IEEE Trans. Veh. Technol., 21*(1), 1–9, 1972.

Zoltowski, M. D., M. Haardt, and C. P. Mathews, Closed-form 2-D angle estimation with rectangular arrays in element space or beamspace via unitary ESPRIT, *IEEE Trans. Signal Process., 44*(2), 316–328, 1996.

K. Araki, J. Takada, and H. Zhu, Department of Electrical and Electronic Engineering, Tokyo Institute of Technology, 2-12-1 O-okayama, Meguro-ku, Tokyo 152-8552, Japan. (tony@icc.titech.ac.jp)

T. Kobayashi, YRP Mobile Telecommunications Key Technology Research Laboratories Co., Ltd., Building 1, 6th floor, YRP Center, 3-4, Hikarinoka, Yokosuka 239-0847, Japan.

(Received April 22, 1999; revised July 17, 2000; accepted August 7, 2000.)